

## Collisional spreading of Enceladus' neutral cloud

T.A. Cassidy\*, R.E. Johnson

Charlottesville, Virginia, United States

### ARTICLE INFO

#### Article history:

Received 4 February 2010

Revised 2 April 2010

Accepted 12 April 2010

Available online 21 April 2010

#### Keywords:

Enceladus

Saturn, Magnetosphere

Satellites, Atmospheres

### ABSTRACT

We describe a direct simulation Monte Carlo (DSMC) model of Enceladus' neutral cloud and compare its results to observations of OH and O orbiting Saturn. The OH and O are observed far from Enceladus (at 3.95  $R_S$ ), as far out as 25  $R_S$  for O. Previous DSMC models attributed this breadth primarily to ion/neutral scattering (including charge exchange) and molecular dissociation. However, the newly reported O observations and a reinterpretation of the OH observations (Melin, H., Shemansky, D.E., Liu, X. [2009] *Planet. Space Sci.*, 57, 1743–1753, PS&S) showed that the cloud is broader than previously thought. We conclude that the addition of neutral/neutral scattering (Farmer, A.J. [2009] *Icarus*, 202, 280–286), which was underestimated by previous models, brings the model results in line with the new observations. Neutral/neutral collisions primarily happen in the densest part of the cloud, near Enceladus' orbit, but contribute to the spreading by pumping up orbital eccentricity. Based on the cloud model presented here Enceladus maybe the ultimate source of oxygen for the upper atmospheres of Titan and Saturn. We also predict that large quantities of OH, O and H<sub>2</sub>O bombard Saturn's icy satellites.

© 2010 Elsevier Inc. All rights reserved.

### 1. Introduction

The vast cloud of neutral OH orbiting Saturn, discovered by Shemansky et al. (1993), was long thought to come from H<sub>2</sub>O sourced somewhere near Enceladus' orbit (e.g., Jurac et al., 2002; Jurac and Richardson, 2005). The discovery of Enceladus' plumes identified that source and in the expected quantity. Jurac and Richardson (2005) estimated, based on a series of remote OH cloud observations, that Enceladus produced on the order of 10<sup>28</sup> H<sub>2</sub>O s<sup>-1</sup>. This is about the same as the most recent estimates from in situ Cassini data (e.g., Smith et al., 2010). The models of Jurac and coworkers also seemed to reproduce the breadth of the OH cloud by including several spreading processes:

- **Charge exchange:** The plasma in Saturn's magnetosphere (e<sup>-</sup>, O<sup>+</sup>, OH<sup>+</sup>, H<sub>2</sub>O<sup>+</sup>, H<sub>3</sub>O<sup>+</sup>, H<sup>+</sup>) roughly co-rotates with Saturn. The difference between plasma flow speed and local circular orbit speed (i.e., that of a water molecule that just left Enceladus) is about 20 km s<sup>-1</sup> near Enceladus' orbit (Wilson et al., 2009). An ion can be neutralized by exchanging charge with an orbiting neutral. Since the plasma and neutrals are both primarily water group (O, OH, H<sub>2</sub>O) this process is roughly equivalent to adding ~20 km s<sup>-1</sup> to the orbiting neutral, fast enough to escape Sat-

urn's gravity. There is actually a range of ion/neutral relative speeds due to the high ion temperatures. A significant fraction of charge exchange events even result in a slowed neutral.

- **Ion/neutral scattering:** The ions and neutrals also exchange momentum, causing deflections whether or not a charge exchange occurs (e.g., Johnson et al., 2006a).
- **Molecular dissociation:** Magnetospheric electrons and solar UV photons dissociate H<sub>2</sub>O and OH into fast-moving fragments. The fragments with O atoms can gain on the order of 1 km s<sup>-1</sup> in a random direction.

Despite the success of these models, two recent developments prompted us to revisit the problem. Melin et al. (2009) published Cassini UVIS (UV Imaging Spectrometer) data showing an atomic oxygen cloud much broader than the OH cloud. In that same paper they also reevaluated the OH observations and concluded that the OH cloud is broader than previously thought. Concomitantly, Cassini plasma measurements suggested a source of water product ions further out in Saturn's magnetosphere than initially thought (Rymer et al., 2007; Persoon et al., 2009). The other development came from Farmer (2009), who showed that neutral/neutral collisions could be responsible for much of the radial spreading. The proposed mechanism is illustrated in Fig. 1. The orbiting cloud is, to first order, made up of molecules on nearly circular Keplerian orbits. Neutral/neutral collisions create viscosity, and that viscosity transfers momentum from the relatively fast orbits of the inner cloud to the relatively slow orbits further out. The result is that the inner cloud moves inward and the outer cloud moves outward.

\* Corresponding author. Present address: California Institute of Technology, Jet Propulsion Laboratory, 4800 Oak Grove Dr, MS 183-601, Pasadena, CA 91109, United States.

E-mail address: [timothy.a.cassidy@jpl.nasa.gov](mailto:timothy.a.cassidy@jpl.nasa.gov) (T.A. Cassidy).

Collisions between molecules provide viscosity:

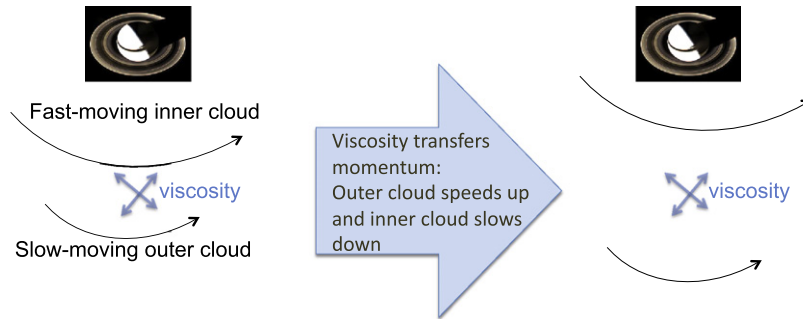


Fig. 1. Schematic of the viscous spreading mechanism: viscosity, provided by neutral/neutral collisions, transfers momentum between molecules on adjacent orbits.

Jurac et al. (2002) and Jurac and Richardson (2005, 2007) included neutral/neutral collisions but underestimated the collision cross sections. They modeled all such collisions as repulsive collisions between atomic oxygen atoms, but the permanent electric dipoles of OH and H<sub>2</sub>O result in long-range interactions and thus larger cross sections.

Farmer (2009) modeled the viscous spreading mechanism while neglecting the other spreading mechanisms described above. Here we present a direct simulation Monte Carlo (DSMC) model with the combined effects of neutral/neutral collisions and the plasma/UV processes listed above. We conclude that both are necessary to reproduce the observations of Melin et al. (2009), though the neutral/neutral collisions contribute to the spreading in an unexpected way. We also show the additional spreading has important implications for the atmospheres of Titan and Saturn.

## 2. Model description

“Direct Simulation” refers to the direct simulation of particle trajectories. Instead of treating the gas as a fluid, we model it as a collection of individual atoms and molecules. A direct simulation approach is required when the mean free path between collisions is comparable to or larger than relevant length scales (Bird, 1994), as illustrated in Fig. 2. A fluid approach, such as that used by Farmer (2009), is not appropriate since a water molecule orbiting in the thickest part of Enceladus’ neutral cloud collides only once per orbit (Fig. 3).

The DSMC model is an extension of our previous Monte Carlo modeling (Johnson et al., 2006a; Cassidy et al., 2007, 2008) modified to include collisions between “test particles,” the several million particles that stand in for the neutral gas cloud. The test particles are followed as they orbit Saturn (we assume ideal Keplerian orbits), and the trajectories are used to calculate densities in

DSMC, unlike continuum fluid dynamics, follows the motion of individual molecules:

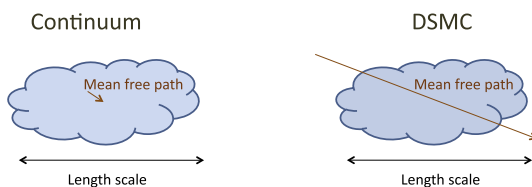


Fig. 2. Schematic of DSMC criterion. A fluid model requires that the mean free path be much smaller than any relevant length scale.

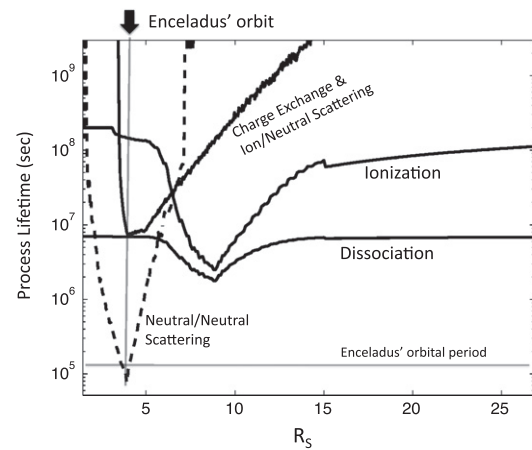


Fig. 3. Lifetimes for model processes at Saturn’s ring plane as a function of distance from Saturn. The collision lifetime was calculated for collisions with a center of mass scattering angle  $\chi$  greater than 0.1 radians ( $6^\circ$ ).

“collision cells”, volumes over which the average density is calculated. The collision cells are rectangles in spherical coordinates,  $2^\circ$  in the  $\theta$  direction,  $10^\circ$  in the  $\phi$  direction and  $3 \times 10^3$  km in the radial direction. As a particle travels through one of these cells the probability of collision is periodically calculated. If a collision is chosen (randomly, hence the term “Monte Carlo” in DSMC) then another particle from the collision cell is chosen (randomly) to be a collision partner. The collision probabilities actually depend on relative particle speed, so the program actually has to calculate the collision probabilities twice: The first calculation uses an assumed maximum collision probability. The actual probability is calculated after a collision partner is chosen (randomly) and the relative speed calculated. If a collision is found to occur then new trajectories are calculated based on the collision details described later in this section.

Details of DSMC modeling are in Bird (1994), but there are two peculiar features of our model. First, our model calculates trajectories and densities in a reference frame that rotates with Enceladus’ orbit. In this reference frame the H<sub>2</sub>O source is fixed in space and so the orbit of Enceladus does not introduce time-variability. The plume itself is unpredictably time-variable, but we did not consider that complication for this paper (see, e.g., Smith et al., 2010). The other peculiarity occurs when we collide two particles in a collision cell. In reality collisions only happen when two particles are close to one another, but in this model the two particles can be separated by up to  $10^\circ$  in the  $\phi$  direction. This presents a potential problem: two particles traveling at nearly same speed in

circular orbits have, at  $10^\circ$  separation, quite high relative speed. Since these are representative test particles we fix this problem by rotating both particles to the same  $(\phi, \theta)$  position before the collision. They are rotated back to their original positions after the collision. A similar problem arises in the radial direction, which we dealt with by keeping the collision cells as small as possible. One possible criterion for radial cell size is that the difference between circular orbit speeds ( $\propto r^{-1/2}$ ) at the inner and outer cell boundaries be much less than the gas velocity dispersion.

Applying this criterion to a cold gas results in very small radial cell sizes, on the order of  $10^3$  km, much less, for example, than the cell sizes in Marconi (2003). The ultimate size criterion, however, is that the simulation results not change with cell size, and we found that cell sizes much larger than  $10^3$  km did not change the results. This is likely attributable to the fact that the orbits are not circular, but quite eccentric. The average eccentricity in our model is 0.5, as discussed below.

### 2.1. Lifetimes

As the program follows a test particle through its orbit around Saturn, it periodically checks the probability that one of the above processes will happen. For a given period of time  $\Delta t$  the probability of a process happening is given by

$$1 - \exp(-\Delta t/\tau)$$

a standard statistical result where  $\tau$  is the lifetime for one of the processes described above. The lifetimes for various processes, as a function of distance from Saturn, are shown in Fig. 3.

The loss processes are ionization (our model does not track ions), escape from an arbitrary outer boundary ( $60 R_S$ ), loss to Saturn's atmosphere and sticking to the main rings. We assume that all species tracked by the program stick permanently to the rings. Since the rings have finite optical depth, many particles travel straight through the rings without encountering a surface. The probabilities are described in Johnson et al. (2006b).

### 2.2. Source rate

The  $H_2O$  source rate is our model's only free parameter. The  $H_2O$  source rate at Enceladus' orbit has been estimated since the discovery of Saturn's OH cloud (see summary in Johnson et al. (2006a)). The estimates are uncertain, and the source rate varies (Smith et al., 2010), but is on the order of  $1 \times 10^{28} H_2O s^{-1}$  (e.g., Smith et al., 2010). For our model results below, we settled on  $1.0 \times 10^{28} H_2O s^{-1}$ , as this best matched the atomic oxygen observations (Melin et al., 2009). Though Jurac and coworkers concluded that Enceladus was the dominant source of  $H_2O$  in the Saturn system, they used multiple sources to match the OH observations. Here our only source is Enceladus.

The details of the ejected plume, such as geometry and exact flow speed, have been studied extensively (e.g., Hansen et al., 2008; Smith et al., 2010), but are not particularly important for large-scale torus modeling. The breadth of the torus is due to the various processes described above, not ejection speed. As in Johnson et al. (2006a) we modeled the ejection as a southward-facing sublimating 180 K ice, i.e., the Maxwell "flux" distribution, the Maxwell–Boltzmann distribution times molecule speed. The result is a gas with an average outward speed of  $540 m s^{-1}$ . Such a source is, very roughly, similar to more detailed plume models (Smith et al., 2010).

### 2.3. Neutral/neutral collisions

Since DSMC calculates the trajectories of individual molecules, rather than treating the gas as a fluid, it requires a detailed descrip-

tion of the collisions in the form a differential cross section<sup>1</sup>  $d\sigma/d\Omega$  from which we can calculate the center of mass reference frame scattering angle<sup>2</sup>  $\chi$ . A purely fluid description only requires the relevant macroscopic properties such as viscosity.

We calculated  $d\sigma/d\Omega$  using an inverse cube potential, which is appropriate for two interacting permanent dipoles (Johnson, 1990). We used the simplifying assumption of small-angle scattering (Johnson, 1990), which is appropriate for the vast majority of  $H_2O/H_2O$  collisions in our model. The large dipole/dipole cross section means that most interactions are distant and result in only slight deflections. For inverse power potentials (potential proportional to  $r^{-n}$ ), the differential cross section can be approximated

$$d\sigma/d\Omega \propto (u^{-4/n})(1 - \cos(\chi))^{-(1+1/n)} \quad (1)$$

where  $u$  is the relative speed between colliding  $H_2O$  molecules and  $n = 3$  for dipole/dipole scattering. Eq. (1) can be derived from the expressions in Johnson (1990); specifically, Table 2.1 and Appendix B of Chapter 2.

The total cross section is found by integrating Eq. (1):

$$\sigma_T = \int d\sigma/d\Omega d\Omega \quad (2)$$

Integrating over  $4\pi$  steradians produces an infinite cross section, a well-known property of the inverse power law potential. Specifically, Eq. (2) goes to infinity as the lower bound of integration  $\chi \rightarrow 0$ . Our program, of course, requires a finite cross section. We get a finite cross section by using an angular cutoff,<sup>3</sup> we only include scattering angles  $\chi$  greater than some small angle  $\chi_0$ .

The absolute value of the cross section was found, as in Farmer (2009), using the water vapor viscosity measurements of Teske et al. (2005). Farmer (2009) derived a viscosity cross section from that data using a simple relation between cross section and viscosity. The viscosity cross section is defined by Bird (1994) as

$$\sigma_\mu = \int \sin^2(\chi)(d\sigma/d\Omega)d\Omega \quad (3)$$

Eq. (3) is finite when evaluated with Eq. (1), unlike the total cross section (Eq. (2)). Given the experimentally-derived viscosity cross section, we used the expressions above to relate the total scattering and viscosity cross sections:

$$\begin{aligned} \sigma_T(\chi_0) &= \int_{\chi_0}^{\pi} d\sigma/d\Omega d\Omega \\ &= \sigma_\mu \frac{2 - 3/n + (1/n)^2}{2^{2-1/n}(1/n)} \left\{ \frac{1}{(1 - \cos(\chi_0))^{1/n}} - \frac{1}{2^{1/n}} \right\} \end{aligned} \quad (4)$$

where  $\pi$  is the maximum scattering angle and  $\chi_0$  is the angular cutoff mentioned above, the minimum scattering angle. We chose  $\chi_0 = 0.1$  radians ( $5.7^\circ$ ). Changing this to smaller angles does not significantly affect the cloud morphology. Plugging this cutoff and  $n = 3$  (inverse cube scattering) into Eq. (4) yields

$$\sigma_T(\chi_0) = 5.3\sigma_\mu \quad (5)$$

which gives us the total scattering cross section in terms of an experimentally determined viscosity cross section. Since Farmer (2009) did not distinguish between the viscosity and total cross sections, we use a much larger total scattering cross section, though the viscosity of our two models should, in principle, be the same.

<sup>1</sup> Note that the differential cross section  $d\sigma/d\Omega$  is often denoted  $\sigma$  in the relevant literature.  $\sigma$  is also sometimes used for the diameter of the molecule.

<sup>2</sup> Note that  $\Omega$  is the solid scattering angle and  $d\Omega = d\phi d\cos(\chi)$ , where  $\phi$  is the azimuthal angle.

<sup>3</sup> A quantum calculation for scattering at very small angles, the diffraction regime, gives a finite cross section for  $n > 2$ .

Farmer (2009) estimated  $\sigma_\mu$  from the water vapor viscosity measurements of Teske et al. (2005):

$$\sigma_\mu = 80(u/500 \text{ m s}^{-1})^{-4/3} \text{ \AA}^2 \quad (6)$$

The speed dependence came about from theoretical considerations, notice that it is the same as Eq. (1), but is also consistent with the data. Teske et al. found that the viscosity varied with temperature as  $T^{-2/3}$ , the square of the speed dependence in Eq. (6).

It is useful to pause here and ask: to what extent do the details above matter to the final model results? For example, what if we replace the detailed treatment above with a “hard sphere” approximation in place of Eq. (1)? In that case the water molecules are treated as elastic spheres; which makes the collision process simpler in concept and easier to implement, but produces relatively large scattering angles. Qualitatively, we found similar results with “hard sphere” scattering in place of Eq. (1), but only if we use  $\sigma_\mu$  in place of the total scattering cross section (as in Farmer (2009)). The smaller cross section, combined with the large scattering angles of hard sphere collisions, produced results similar to the combination of small scattering angles (Eq. (1)) and much larger  $\sigma_T$ . The importance of collision details for fluid properties are discussed extensively in Bird (1994).

Eqs. (5) and (6), along with calculated H<sub>2</sub>O densities, are used by the DSMC program to calculate collision probabilities. Once the program decides to collide two molecules a scattering angle  $\chi$  is chosen via a Monte Carlo procedure. A random number generator produces a number  $R$  between 0 and 1 with uniform probability. We calculate  $\chi$  from the following formula

$$\frac{\sigma_T(\chi)}{\sigma_T(\chi_0)} = R \quad (7)$$

and solving for  $\chi$ .

Our model includes collisions involving OH and O in addition to H<sub>2</sub>O; they are produced by photodissociation and electron-impact dissociation. Since OH and H<sub>2</sub>O have similar dipole moments and masses, they are treated identically. Any collision involving an O atom was given the cross section of an O/O collision, which we estimated using the O atom Van der Waals radius to give a total collision cross section of 28 Å<sup>2</sup> (Bondi, 1964). This is much smaller than the cross sections described above (Eqs. (5) and (6)). The cross section of any non-polar atom is fairly constant across a wide range of speeds (Bird, 1994, p. 93; Tully and Johnson, 2001). We used isotropic (hard sphere) scattering for these collisions, for which  $d\sigma/d\Omega = \text{constant}$ , instead of Eq. (1) (e.g., Bird, 1994). Future work might include non-isotropic differential cross sections; Tully and Johnson (2001, Fig. 2) showed that O/O collisions become less isotropic as collision energy increases.

#### 2.4. Charge exchange and ion/neutral scattering

The charge exchange rate is given by

$$v_{\text{CE}} = n \int_{u=0}^{\infty} \sigma_{\text{CE}}(u) u f(|\vec{u} - \vec{u}_{\text{plasma}}|) du \quad (8)$$

where  $f$  is the Maxwell–Boltzmann distribution (non-isotropic as described below) for the given ion temperature,  $u$  is the relative speed between the neutral and ion, and  $\vec{u}_{\text{plasma}}$  is the plasma flow velocity relative to the neutral.

The program implements the collision by first generating a random velocity for the ion from the expression

$$R = \int_{-\infty}^{u_i} \sigma_{\text{CE}}(u) |u| f(x - u_{\text{plasma},i}) dx / \int_{-\infty}^{\infty} \sigma_{\text{CE}}(u) |u| f(x - u_{\text{plasma},i}) dx$$

where  $i$  is the velocity component,  $x$  is a dummy variable, and  $u_i$  is the randomly-derived ion speed to be solved for after evaluating the

integral (compare with Eq. (7)). Note that the cross section is a function of the total relative speed  $u$  and not just  $u_i$ , a complication we will not discuss.

As for neutral/neutral collisions, we used a differential scattering cross section  $d\sigma/d\Omega$  to calculate ion–neutral scattering angles. We used  $d\sigma/d\Omega$  from Eq. (1) but with  $n \rightarrow \infty$ . The resulting differential cross section approximates more detailed scattering calculations (Tully and Johnson, 2001).<sup>4</sup>

As for the neutral/neutral scattering, we require a minimum scattering angle  $\chi_0$  for use in Eq. (7). For the neutral/neutral collisions above  $\chi_0$  was chosen sufficiently small to not affect the cloud morphology. The total charge exchange cross section, however, is experimentally determined (Eq. (9)), allowing us to use a physically-determined  $\chi_0$ . We can estimate  $\chi_0$  from the uncertainty principle. The minimum momentum change during a collision is given by  $\Delta p = h/2\Delta l$ , where  $\Delta l$  is the uncertainty in position. Combining this with a relation between momentum and scattering angle,  $\Delta p \approx p_0 \chi$ , where  $p_0$  is the center of mass reference frame momentum, yields

$$\chi_0 = \frac{h/2m\Delta l}{u} \approx \frac{70 \text{ m s}^{-1}}{u}$$

where  $m$  is the reduced mass, approximately one-half the mass of a water molecule,  $\Delta l$  is approximately one Bohr radius, and  $u$ , as before, is the relative collision speed. Johnson (1982) discusses the exact cutoff for an explicit quantum mechanical calculation (for a specific interatomic potential) and finds nearly the same result.  $\chi_0$  in any case, is quite small, as  $u$  is typically much greater than 70 m s<sup>-1</sup>.

The value of the charge exchange cross section is potentially quite complicated since it depends on the species involved. Since all measured water group charge exchange cross sections are similar, we assumed that all combinations of water group species have the same speed-dependent cross section. The differences between different reactions are much less than an order of magnitude for the data available; e.g. compare Dressler et al. (1996), Fig. 3, with Lishawa et al. (1990), Fig. 7. This approach also neglects other ion/neutral reactions with much smaller cross sections.

For the energy range of interest, we used the following expression for the charge exchange cross section as a function of neutral/ion relative energy:

$$\sigma_{\text{CE}} = 2 \times 10^{-14.8} E^{-0.18} \text{ cm}^2 \quad (9)$$

where  $E$  is the center of mass reference frame energy of the ion/neutral system. Except for the factor of 2, which will be explained shortly, this is a fit to the experimentally measured cross sections for the reaction  $\text{H}_2\text{O}^+ + \text{H}_2\text{O} \rightarrow \text{H}_2\text{O}^+ + \text{H}_2\text{O}$  above  $\sim 1$  eV (Lishawa et al., 1990). The factor of 2 accounts for the fact that the measured charge exchange cross section does not include ion/neutral collisions that just exchange momentum. In the relevant collision energy range, the total ion/neutral collision cross section is about twice the charge exchange cross section (Johnson, 1990). Thus the program randomly decides whether or not charge is exchanged during a collision; there is an equal probability that either the ion or neutral will leave as a neutral. We do not follow the course of the exiting ion, of course; we are only concerned here with the effect of plasma on the neutrals and not vice versa.

The rest of this section describes the many parameters that go into the calculation of the charge exchange rate; various plasma properties that depend on position within the magnetosphere: ion density  $n$ , ion temperature, and plasma flow speed. The parameters are derived from in situ Cassini measurements; specifically

<sup>4</sup> Tully and Johnson (2001) were concerned with collisions between neutral O atoms but considered interatomic potentials that are also used for ion/neutral scattering.

by the CAPS (Cassini Plasma Spectrometer) and RPWS (Radio and Plasma Wave Science) instruments. Sittler et al. (2006) estimated the water group ion temperature *perpendicular* to the magnetic field with the following fit:

$$T_{\perp} = 35(L/4)^2 \text{ eV}$$

where  $L$  is the dipole  $L$  shell in Saturn radii. Inside of  $4 R_S$ , we assume a constant temperature (Sittler et al., 2006). The relationship between dipole  $L$ , distance from Saturn's center  $r$ , and magnetic latitude  $\lambda$  is given by

$$L = r / \cos^2(\lambda)$$

The temperature *parallel* to the magnetic field can be derived from measurements of ion density vs. magnetic latitude. The water group ion density peaks at the magnetic equator (the ring plane), and falls off with magnetic latitude according to

$$n_o \exp \left[ \frac{-1}{3} \frac{L^2}{H^2} (1 - \cos^6(\lambda)) \right]$$

where  $n_o$  is the equatorial ion density and  $H_w$  is the water group ion scale height. This formula is derived in Persoon et al. (2006). The temperature parallel to the magnetic field is given by

$$T_{\parallel} = (H^2/2)3m\Omega^2$$

where  $m$  is the ion mass and  $\Omega$  is the plasma rotation speed (radians per second). The water group ion scale height is given by the following fit from Persoon et al. (2009):

$$H = 0.045L^{1.5}$$

where  $H_w$  is in units of Saturn radii. The water group ion density at the equator, based on Cassini data analysis by from Persoon et al. (2009) and Sittler et al. (2008), is given by:

|                                   |                         |
|-----------------------------------|-------------------------|
| $0 \text{ cm}^{-3}$               | $(L < 3.5 R_S)$         |
| $50 (2(L - 3.5)) \text{ cm}^{-3}$ | $(3.5 R_S < L < 4 R_S)$ |
| $50 \text{ cm}^{-3}$              | $(4 R_S < L < 5 R_S)$   |
| $60,775L^{-4.3} \text{ cm}^{-3}$  | $(L > 5 R_S)$           |

Similar fits can be found in earlier papers such as Sittler et al. (2006) and Wilson et al. (2009).

The final piece of information needed to calculate charge exchange rates is the plasma flow speed. According to Wilson et al. (2009), the plasma co-rotates with Saturn inward of  $3 R_S$  and lags by about 20% below co-rotation beyond  $4 R_S$ . The lag increases about linearly between 3 and  $4 R_S$ .

## 2.5. Photon and electron impact processes

Solar UV photons and electrons in Saturn's magnetosphere both ionize and dissociate molecules. The lifetimes for photodissociation and photoionization are found in Heubner et al. (1992). There are a range of possible lifetime values for each species due to solar UV variability. E.g., the photoionization lifetime ranges from  $1 \times 10^8$  s to  $3 \times 10^8$  s for  $\text{H}_2\text{O}$ ,  $1 \times 10^8$  s to  $4 \times 10^8$  s for OH, and  $2 \times 10^8$  s to  $4 \times 10^8$  s for O. For simplicity we used a photoionization lifetime of  $2 \times 10^8$  s for all three species.

For photodissociation we used a lifetime of  $7 \times 10^6$  s for  $\text{H}_2\text{O}$  and OH. There are many possible outcomes for the dissociation of  $\text{H}_2\text{O}$ , but the most common result (or 'channel') results in H and OH and an excess kinetic energy of  $\sim 3.7$  eV. We neglected the other channels (<10% level). Conservation of momentum requires that 1/18th of this energy is given as kinetic energy to the OH, with the rest going to the H. This is implemented by giving the newly-formed OH additional kinetic energy in a random direc-

tion (Jurac and Richardson, 2005). For the dissociation of OH into O and H there are two equally probable channels: one results in an O atom with 1/18th of 2.07 eV, the other with 1/18th of 7.73 eV.

Calculation of electron-impact dissociation and ionization rates required cross sections (as a function of electron speed  $u$ ), electron density  $n$  and electron temperature. The electron-impact dissociation or ionization rate is given by

$$v = n \int \sigma(u)uf(u)du$$

where  $f(u)$  is the Maxwell-Boltzmann distribution for the given electron temperature. Unlike the similar Eq. (8), we neglect the plasma flow speed, since it is much less than the thermal electron speed. The cross sections for  $\text{H}_2\text{O}$  dissociation and ionization are given in Itikawa and Mason (2005). We use the same cross sections for OH and, for ionization, O. The ionization cross sections for all three species are quite similar (compare Tarnovsky et al. (1998) and Itikawa and Mason (2005) and [http://physics.nist.gov/cgi-bin/ionization/ion\\_data.php?id=OI&ision=I&initial=&total=Y](http://physics.nist.gov/cgi-bin/ionization/ion_data.php?id=OI&ision=I&initial=&total=Y)). We gave fragments due to electron-impact dissociation the same energy as photodissociated fragments (Jurac and Richardson, 2005).

The electron properties are described in Schippers et al. (2008). There are two populations of electrons: the dense, relatively cold thermal and the tenuous, relatively warm suprathermal. There are also suprathermal ions, but we did not consider them in the previous section as they are a relatively small fraction of the total

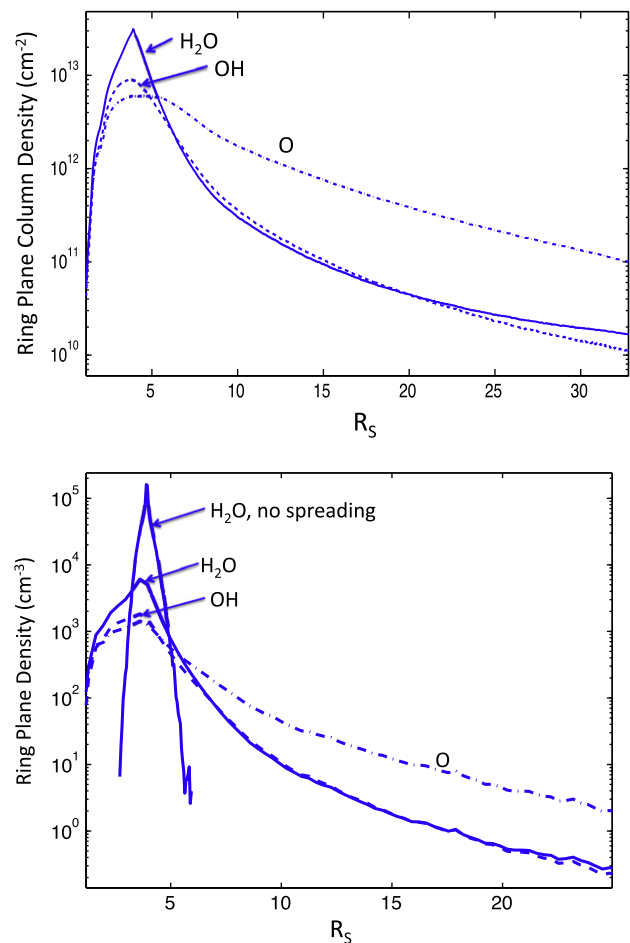


**Fig. 4.** Top: Steady state column density (above and below Saturn's equatorial/ring plane) for the three neutral species in our model.  $\text{H}_2\text{O}$  is the source molecule from which OH and O are subsequently formed. Bottom: Density in Saturn's ring plane. In the hypothetical no-spreading case the breadth of the  $\text{H}_2\text{O}$  torus is due solely to the thermal range of ejection speeds from Enceladus.

and often have smaller charge exchange cross sections. Suprathermal electrons, though, are very important as they have large cross sections and the thermal electron population near Enceladus' orbit is too cold to ionize or dissociate water molecules. Schippers et al. (2008) characterized the two populations; giving their temperature and density, but not considering their variation with magnetic latitude. Without knowledge of latitudinal variation, we gave both populations the same variation with latitude by equating the electron density to the sum of the water group ion density (discussed above) and the hydrogen ion density (Persoon et al., 2009).

### 3. Results

The model results are shown in Figs. 4–6. Fig. 4 shows the steady-state densities for the three water group species in our model. It takes about one photoionization lifetime ( $2 \times 10^8$  s) to reach steady state. The model results are compared to data in Fig. 5. The data are OH and O line-of-sight column densities derived from observations of reflected UV light. In the case of OH, the data came from Hubble Space Telescope observations in the 1990s and in the case of O, Cassini UVIS (Ultraviolet Spectrometer) observations from 2003 to 2005. Both were reported in Melin et al. (2009). The error bars for the OH data were set to a factor of 3 based on the raw data

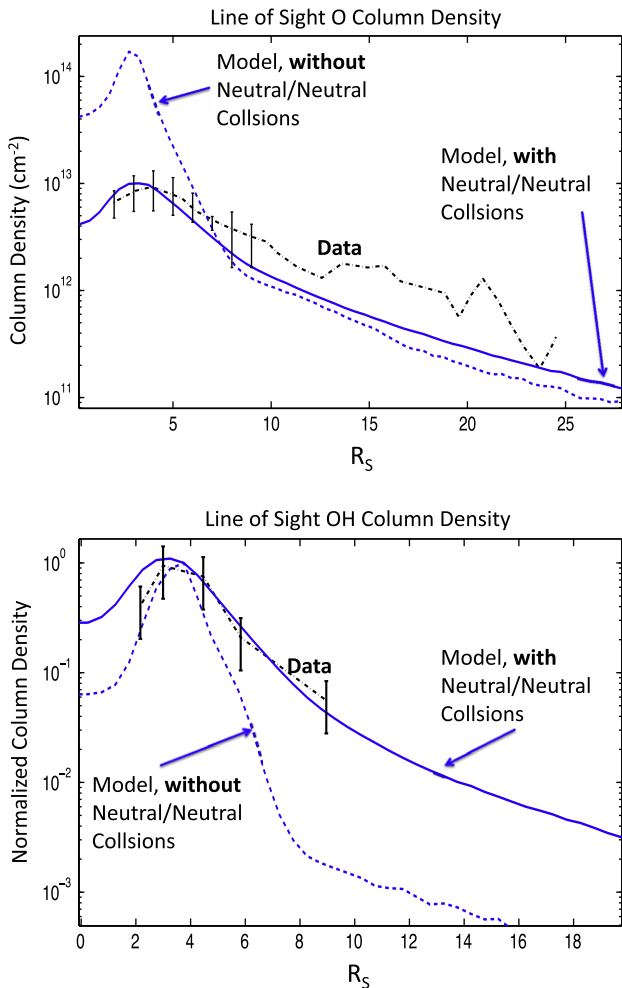


**Fig. 5.** Comparison of modeled *line-of-sight* column densities with observations from Melin et al. (2009). The OH column density was normalized to 1 at  $4 R_S$  in the absence of an absolute scale. Note that the O cloud is much broader than the OH cloud and that the OH profile is slightly different than that used by previous modelers, as discussed in the introduction.

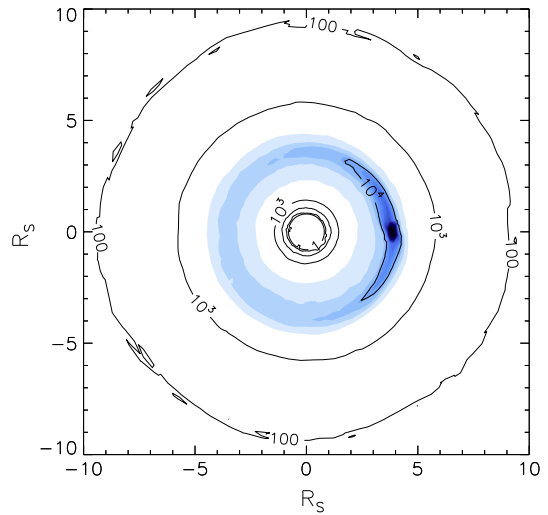


**Fig. 6.** Top down view of calculated neutral water group ( $H_2O$ , OH and O) density at Saturn's ring plane. The contours indicate density in units of  $cm^{-3}$ . The contour lines show the density in factor of 10 increments, while the shading is on a linear scale to show structure in the dense part of the cloud near Enceladus' orbit. The highest density, the dark spot on the right-hand side, is near Enceladus itself. The characteristic "banana" shape is just barely visible in the  $10^4 cm^{-3}$  contour.

from Jurac and Richardson (2005, Fig. 1). There are no comparable observations of  $H_2O$  in the Saturn system.  $H_2O$  densities have only been measured in the immediate vicinity of Enceladus.

Two model results are included for comparison with the data, one with neutral/neutral collisions and one without. The cases without are qualitatively similar to modeling work of Jurac and Richardson (2005) and Johnson et al. (2006a,b). For both species, neutral/neutral collisions are critically important to reproducing the data at the source rate chosen here. The OH and O clouds are well within the error bars, where there are error bars. There were no error bars published for the O cloud beyond  $10 R_S$ . Out beyond this distance, the modeled O column density is about a factor of 2 lower than the data. The discrepancy could result from one of the many approximations in our model, such as the treatment of all plasma/neutral interactions using generic "water group" cross sections. Another possibility, explored by Jurac and coworkers, is that the icy satellites beyond Enceladus are also a source of  $H_2O$ .

Fig. 6 shows the azimuthal structure in the neutral cloud at Saturn's equatorial plane. The densities are highest near Enceladus, of course, but the asymmetry is not as pronounced as for Io's neutral cloud, where neutral lifetimes are much shorter. As for the neutral clouds produced by Io and Europa, the model predicts a "banana" shaped cloud (Burger and Johnson, 2004; Smyth and Marconi, 2006).

An important result from Fig. 3 is the narrowness of the neutral/neutral collision lifetime curve. Though the neutral cloud extends beyond  $25 R_S$ , and neutral/neutral collisions are critical for populating it, the collisions are confined to a relatively narrow ring

**Table 1**  
Comparison to previous model results.

| Loss process                | Jurac and Richardson (2007) | Johnson et al. (2006a,b) | Current model        |
|-----------------------------|-----------------------------|--------------------------|----------------------|
| Lost to main rings          | 17%                         | 18%                      | 36%                  |
| Lost to Saturn's atmosphere | 10%                         |                          | 7%                   |
| Escaped outer boundary      | 34%                         | 44%                      | 31%                  |
| Ionized                     | 38%                         | 38%                      | 26%                  |
| Source rate                 | $1.0 \times 10^{28}$        | $5.0 \times 10^{27}$     | $1.0 \times 10^{28}$ |

**Table 2**  
Water group neutral (H<sub>2</sub>O/OH/O) flux onto Saturn's largest icy satellites, estimated without gravitational focusing. Each column lists the peak flux onto the indicated hemisphere. Note that Enceladus is at 3.95 R<sub>S</sub>. The water group ion flux was calculated using parameters described earlier in paper.

| Moon                      | Trailing<br>cm <sup>-2</sup> s <sup>-1</sup> | Leading<br>cm <sup>-2</sup> s <sup>-1</sup> | Sub-Saturnian<br>cm <sup>-2</sup> s <sup>-1</sup> | Anti-Saturnian<br>cm <sup>-2</sup> s <sup>-1</sup> | North Pole<br>cm <sup>-2</sup> s <sup>-1</sup> | South Pole<br>cm <sup>-2</sup> s <sup>-1</sup> | Ion Flux (peaks on<br>trailing hemisphere)           |
|---------------------------|--|---|---|--|--|--|--|
| Mimas 3.1 R <sub>S</sub>  | 6 × 10 <sup>8</sup>                          | 5 × 10 <sup>8</sup>                         | 1 × 10 <sup>9</sup>                               | 1 × 10 <sup>9</sup>                                | 7 × 10 <sup>8</sup>                            | 7 × 10 <sup>8</sup>                            | 0 cm <sup>-2</sup> s <sup>-1</sup>                   |
| Tethys 4.9 R <sub>S</sub> | 1 × 10 <sup>8</sup>                          | 4 × 10 <sup>8</sup>                         | 5 × 10 <sup>8</sup>                               | 5 × 10 <sup>8</sup>                                | 3 × 10 <sup>8</sup>                            | 3 × 10 <sup>8</sup>                            | 1 × 10 <sup>8</sup> cm <sup>-2</sup> s <sup>-1</sup> |
| Dione 6.3 R <sub>S</sub>  | 1 × 10 <sup>7</sup>                          | 1 × 10 <sup>8</sup>                         | 1 × 10 <sup>8</sup>                               | 1 × 10 <sup>8</sup>                                | 6 × 10 <sup>7</sup>                            | 6 × 10 <sup>7</sup>                            | 7 × 10 <sup>7</sup> cm <sup>-2</sup> s <sup>-1</sup> |
| Rhea 8.7 R <sub>S</sub>   | 2 × 10 <sup>6</sup>                          | 4 × 10 <sup>7</sup>                         | 3 × 10 <sup>7</sup>                               | 3 × 10 <sup>7</sup>                                | 1 × 10 <sup>7</sup>                            | 1 × 10 <sup>7</sup>                            | 3 × 10 <sup>7</sup> cm <sup>-2</sup> s <sup>-1</sup> |
| Titan 20.2 R <sub>S</sub> | 1 × 10 <sup>5</sup>                          | 3 × 10 <sup>6</sup>                         | 8 × 10 <sup>5</sup>                               | 8 × 10 <sup>5</sup>                                | 4 × 10 <sup>5</sup>                            | 4 × 10 <sup>5</sup>                            | See Hartle et al. (2006)                             |

around Enceladus' orbit. The collisions near Enceladus' orbit affect the broader cloud due to the high eccentricities and semimajor axes of the test particles; particles in elliptic orbits that reach distances as large as 25 R<sub>S</sub> still have collisions near 4 R<sub>S</sub>. This method of spreading contrasts with the Farmer (2009) fluid viscous spreading model in Fig. 1, in which particles have relatively small eccentricities and collisions happen throughout the cloud.

The spreading works as follows: particles begin with a slight eccentricity and inclination after leaving Enceladus due to the distribution of ejection speeds and directions. This results in particles with nearly identical speeds but slightly different orbits. When these orbits intersect, as mentioned earlier, the relative speeds can be quite high. These collisions scatter particles into orbits with a wider variety of eccentricities, inclinations and semimajor axes, resulting in even higher relative speeds. These higher relative speeds result in a yet wider distribution of orbits. Smyth and Marconi (1993) summarized the relevant research up until that time and described the process as follows: "each elastic atom-atom collision extracts energy from the ordered (azimuthal) motion and transfers this energy into random motion." The key word here is "elastic". The elastic collisions between molecules in our models result in the expansion of the cloud, whereas inelastic collisions in Saturn's main rings do the opposite.

#### 4. Conclusions

Here we have simulated the evolution of the water molecules vented from Enceladus' south pole. We have shown that the interaction of neutrals with magnetospheric plasma and UV photons is important in determining the cloud morphology, as expected based on earlier modeling. What is surprising is that, as suggested by Farmer (2009), neutral-neutral collisions are required to obtain a cloud composition and morphology consistent with the recent observations of the extended O cloud. Because the Enceladus source is variable (Smith et al., 2010) and the neutral-neutral collisions depend on the square of the density, the spatial morphology is likely to change gradually over time.

This neutral cloud appears to be the principle source of plasma in Saturn's magnetosphere and its morphology and composition are critical to understanding plasma properties (Pontius and Hill, 2009; Fleshman et al., 2010). The breadth of the neutral cloud means that it is a source of water products for other objects in the saturnian system. The fate of water products in our model is shown in Table 1. Here we find, consistent with earlier work, that much of Enceladus' outgassed water is accreted onto Saturn's main rings (Jurac and Richardson, 2007; Farrell et al., 2008; Tseng et al., 2010). This might produce the observed UV-bright outer rings as suggested by Jurac and Richardson (2007) and may act to sustain the ring lifetime.

O-containing compounds in Saturn's upper atmosphere also require an external source of ~10<sup>27</sup> O/s (Moses et al., 2000). Based Table 1 and the source rate used here, Enceladus supplies the necessary O: ~10<sup>27</sup> O/s for the source rate used here. Tseng et al.

(2010) estimated a lower bound to the O source originating from Saturn's ring's and found it to be about an order of magnitude smaller, though recycling process are such that it could be the same order of magnitude (Johnson et al., 2006b). Therefore, it appears that O-containing species from Enceladus and the main rings can adequately account for the oxygen in Saturn's thermosphere.

The neutral cloud modeled here has significant densities out past Titan's orbit and is, in fact, a larger source of neutrals at Titan's orbit than Titan itself. This is in contrast to Voyager-era conclusions that Titan itself had a significant neutral torus of its own (Shemansky and Hall, 1992). Smith et al. (2007), e.g., were the first to show that the dominant source of nitrogen in Saturn's magnetosphere is Enceladus and not Titan's own N<sub>2</sub> atmosphere. In addition, Hartle et al. (2006) first showed that the dominant heavy ions at Titan's orbit were water product ions and not ions formed by escape of methane or nitrogen from Titan.

The O density at Titan's orbit is so large that it is also a significant source of O to Titan's upper atmosphere. Our model did not include Titan's gravity, so we could not directly calculate the flux of O into Titan's atmosphere. We can estimate it, though, based on the O density, 5–20 cm<sup>-3</sup>, and its average speed relative to Titan, 2.8 km s<sup>-1</sup>. The lower end of the density range is from our model (Fig. 5) and the upper end is from the Melin et al. (2009) interpretation of the observations. The final piece of information needed is Titan's gravitational focusing, which increases the flux by a factor of about 1.7 (Öpik, 1951),<sup>5</sup> to yield a neutral O flux of 1–5 × 10<sup>24</sup> s<sup>-1</sup> onto Titan's upper atmosphere. This source is comparable to or larger than other sources of O, such as magnetospheric O<sup>+</sup> ions (Hartle et al., 2006) or micrometeorite dust (see summary in Sittler et al. (2009)). An external oxygen flux of this magnitude is needed to account for O-containing species detected in Titan's atmosphere.

The modeled O atoms hit Titan's leading hemisphere. The same pattern holds for all other moons outside of Enceladus' orbit, while inside of Enceladus' orbit the bombardment of water group neutrals is on the moons' trailing hemispheres. This slow deposition of water molecules on the leading hemisphere could contribute to the relatively bright leading hemispheres of Tethys, Dione and Rhea, which have orbits outside Enceladus. Likewise for the bright trailing hemisphere of Mimas, which orbits interior to Enceladus. The predicted bombardment rates are listed in Table 2 for a variety of moons. The bombardment patterns onto the large icy moons are more complicated than at Titan, and so precludes the use of a gravitational focusing factor. E-ring grains have a similar bombardment pattern on the same satellites (Hamilton and Burns, 1994) and have been suggested to brighten the surfaces they bombard (Verbiscer et al., 2007), so further work is needed to distinguish between the effects of gas and grain bombardment. Electron and ion bombardment also contribute to hemispheric asymmetries (Schenk et al., 2010).

<sup>5</sup> This factor is given by  $1 + (v_{esc}/v)^2$ , where  $v_{esc}$  is Titan's escape speed, 2.1 km s<sup>-1</sup> at Titan's exobase.

## References

- Bird, G.A., 1994. *Molecular Gas Dynamics and the Direct Simulation of Gas Flows*. Clarendon Press, New York.
- Bondi, A., 1964. Van der Waals Volumes and Radii. *J. Phys. Chem.* 68 (3), 441–451. doi:10.1021/j100785a001.
- Burger, M.H., Johnson, R.E., 2004. Europa's neutral cloud: morphology and comparisons to Io. *Icarus* 171, 557–560.
- Cassidy, T.A., Johnson, R.E., McGrath, M.A., Wong, M.C., Cooper, J.F., 2007. The spatial morphology of Europa's near-surface O<sub>2</sub> atmosphere. *Icarus* 191, 755–764.
- Cassidy, T.A., Johnson, R.E., Geissler, P.E., Leblanc, F., 2008. Simulation of Na D emission near Europa during eclipse. *J. Geophys. Res. (Planets)* 113, E02005.
- Dressler, Rainer A., Bastian, Michael J., Levandier, Dale J., Murad, Edmond, 1996. Empirical model of the state-to-state dynamics in near-resonant hyperthermal X<sup>+</sup> + H<sub>2</sub>O charge-transfer reactions. *Int. J. Mass Spectrom. Ion Process.* 159, 245–256.
- Farmer, A.J., 2009. Saturn in hot water: Viscous evolution of the Enceladus torus. *Icarus* 202, 280–286.
- Farrell, W.M., Kaiser, M.L., Gurnett, D.A., Kurth, W.S., Persoon, A.M., Wahlund, J.E., Canu, P., 2008. Mass unloading along the inner edge of the Enceladus plasma torus. *Geophys. Res. Lett.* 35, L02203.
- Fleshman, B.L., Delamere, P.A., Bagenal, F., 2010. A sensitivity study of the Enceladus torus. *J. Geophys. Res. (Planets)* 115, E04007.
- Hamilton, D.P., Burns, J.A., 1994. Origin of Saturn's E ring: Self-sustained, naturally. *Science* 264, 550–553.
- Hansen, C.J., Esposito, L.W., Stewart, A.I.F., Meinke, B., Wallis, B., Colwell, J.E., Hendrix, A.R., Larsen, K., Pryor, W., Tian, F., 2008. Water vapour jets inside the plume of gas leaving Enceladus. *Nature* 456, 477–479.
- Hartle, R.E., and 17 colleagues, 2006. Initial interpretation of Titan plasma interaction as observed by the Cassini plasma spectrometer: Comparisons with Voyager 1. *Planet. Space Sci.* 54, 1211–1224.
- Heubner, W.F., Keady, J.J., Lyon, S.P., 1992. Solar photo rates for planetary atmospheres and atmospheric pollutants. *Astrophys. Space Sci.* 195, 1–294.
- Itikawa, Y., Mason, N., 2005. Cross sections for electron collisions with water molecules. *J. Phys. Chem. Ref. Data* 34, 1–22.
- Johnson, R.E., 1982. *Introduction to Atomic and Molecular Collisions*. Plenum Press, New York.
- Johnson, R.E., 1990. *Energetic Charged-Particle Interactions with Atmospheres and Surfaces*. Springer-Verlag.
- Johnson, R.E., Smith, H.T., Tucker, O.J., Liu, M., Burger, M.H., Sittler, E.C., Tokar, R.L., 2006a. The Enceladus and OH Tori at Saturn. *Astrophys. J.* 644, L137–L139.
- Johnson, R.E., and 12 colleagues, 2006b. Production, ionization and redistribution of O<sub>2</sub> in Saturn's ring atmosphere. *Icarus* 180, 393–402.
- Jurac, S., Richardson, J.D., 2005. A self-consistent model of plasma and neutrals at Saturn: Neutral cloud morphology. *J. Geophys. Res. (Space Phys.)* 110, A09220.
- Jurac, S., Richardson, J.D., 2007. Neutral cloud interaction with Saturn's main rings. *Geophys. Res. Lett.* 34, L08102.
- Jurac, S., McGrath, M.A., Johnson, R.E., Richardson, J.D., Vasyliunas, V.M., Eviatar, A., 2002. Saturn: Search for a missing water source. *Geophys. Res. Lett.* 29, 2172. doi:10.1029/2002GL015855.
- Lishawa, C.R., Dressler, R.A., Gardner, J.A., Salter, R.H.M.E., 1990. Cross sections and product kinetic energy analysis of H<sub>2</sub>O<sup>+</sup>–H<sub>2</sub>O collisions at suprathreshold energies. *J. Chem. Phys.* 93 (5), 3196–3206.
- Marconi, M.L., 2003. Structure and evolution of a quasi-collisional gas torus (case of the Triton hydrogen torus). *Icarus* 166, 410–424.
- Melin, H., Shemansky, D.E., Liu, X., 2009. The distribution of atomic hydrogen and oxygen in the magnetosphere of Saturn. *Planet. Space Sci.* 57, 1743–1753.
- Moses, J.I., Lellouch, E., Beacutезд, B., Gladstone, G.R., Feuchtgruber, H., Allen, M., 2000. Photochemistry of Saturn's atmosphere. II. Effects of an influx of external oxygen. *Icarus* 145, 166–202.
- Öpik, E.J., 1951. Collision probability with the planets and the distribution of planetary matter. *Proc. R. Ir. Acad.* 54A, 165–168.
- Persoon, A.M., Gurnett, D.A., Kurth, W.S., Groene, J.B., 2006. A simple scale height model of the electron density in Saturn's plasma disk. *Geophys. Res. Lett.* 33, L18106.
- Persoon, A.M., and 11 colleagues, 2009. A diffusive equilibrium model for the plasma density in Saturn's magnetosphere. *J. Geophys. Res. (Space Phys.)* 114, A04211.
- Pontius, D.H., Hill, T.W., 2009. Plasma mass loading from the extended neutral gas torus of Enceladus as inferred from the observed plasma corotation lag. *Geophys. Res. Lett.* 36, L23103.
- Rymer, A.M., and 13 colleagues, 2007. Electron sources in Saturn's magnetosphere. *J. Geophys. Res. (Space Phys.)* 112, A02201.
- Schenk, P., Hamilton, D.P., Johnson, R.E., McKinnon, W.B., Paranicas, C., Schmidt, J., Showalter, M.R., 2010. Plasma, plumes and rings: Saturn system dynamics as recorded in the global color patterns on its midsize icy satellites, submitted for publication.
- Schippers, P., and 12 colleagues, 2008. Multi-instrument analysis of electron populations in Saturn's magnetosphere. *J. Geophys. Res. (Space Phys.)* 113, A07208.
- Shemansky, D.E., Hall, D.T., 1992. The distribution of atomic hydrogen in the magnetosphere of Saturn. *J. Geophys. Res.* 97, 4143–4161.
- Shemansky, D.E., Matheson, P., Hall, D.T., Hu, H.-Y., Tripp, T.M., 1993. Detection of the hydroxyl radical in the Saturn magnetosphere. *Nature* 363, 329–331.
- Sittler, E.C., and 15 colleagues, 2006. Cassini observations of Saturn's inner plasmasphere: Saturn orbit insertion results. *Planetary and Space Science* 54, 1197–1210.
- Sittler, E.C., and 18 colleagues, 2008. Ion and neutral sources and sinks within Saturn's inner magnetosphere: Cassini results. *Planet. Space Sci.* 56, 3–18.
- Sittler, E.C., Ali, A., Cooper, J.F., Hartle, R.E., Johnson, R.E., Coates, A.J., Young, D.T., 2009. Heavy ion formation in Titan's ionosphere: Magnetospheric introduction of free oxygen and a source of Titan's aerosols? *Planet. Space Sci.* 57, 1547–1557.
- Smith, H.T., Johnson, R.E., Sittler, E.C., Shappirio, M., Reisenfeld, D., Tucker, O.J., Burger, M., Crary, F.J., McComas, D.J., Young, D.T., 2007. Enceladus: The likely dominant nitrogen source in Saturn's magnetosphere. *Icarus* 188, 356–366.
- Smith, H.T., Johnson, R.E., Perry, M.E., Mitchell, D.G., McNutt, R.L., Young, D.T., 2010. Enceladus plume variability and the neutral gas densities in Saturn's magnetosphere, submitted for publication.
- Smyth, W.H., Marconi, M.L., 1993. The nature of the hydrogen tori of Titan and Triton. *Icarus* 101, 18–32.
- Smyth, W.H., Marconi, M.L., 2006. Europa's atmosphere, gas tori, and magnetospheric implications. *Icarus* 181, 510–526.
- Tarnovsky, V., Deutsch, H., Becker, K., 1998. Electron impact ionization of the hydroxyl radical. *J. Chem. Phys.* 109, 932–936.
- Teske, V., Vogel, E., Bich, E., 2005. Viscosity measurements on water vapor and their evaluation. *J. Chem. Eng. Data* 50, 2082–2087.
- Tseng, W.-L., Ip, W.-H., Johnson, R.E., Cassidy, T.A., Elrod, M.K., 2010. The structure and time variability of the ring atmosphere and ionosphere. *Icarus* 206, 382–389.
- Tully, C., Johnson, R.E., 2001. Low energy collisions between ground-state oxygen atoms. *Planet. Space Sci.* 49, 533–537.
- Verbiscer, A., French, R., Showalter, M., Helfenstein, P., 2007. Enceladus: Cosmic graffiti artist caught in the act. *Science* 315, 815.
- Wilson, R.J., Tokar, R.L., Henderson, M.G., 2009. Thermal ion flow in Saturn's inner magnetosphere measured by the Cassini plasma spectrometer: A signature of the Enceladus torus? *Geophys. Res. Lett.* 36, L23104.